RESEARCH ARTICLE

Pulsatile flows and wall-shear stresses in models simulating normal and stenosed aortic arches

Rong Fung Huang · Ten-Fang Yang · Y.-K. Lan

Abstract Pulsatile aqueous glycerol solution flows in the models simulating normal and stenosed human aortic arches are measured by means of particle image velocimetry. Three transparent models were used: normal, 25% stenosed, and 50% stenosed aortic arches. The Womersley parameter, Dean number, and time-averaged Reynolds number are 17.31, 725, and 1,081, respectively. The Reynolds numbers based on the peak velocities of the normal, 25% stenosed, and 50% stenosed aortic arches are 2,484, 3,456, and 3,931, respectively. The study presents the temporal/spatial evolution processes of the flow pattern, velocity distribution, and wall-shear stress during the systolic and diastolic phases. It is found that the flow pattern evolving in the central plane of normal and stenosed aortic arches exhibits (1) a separation bubble around the inner arch, (2) a recirculation vortex around the outer arch wall upstream of the junction of the brachiocephalic artery, (3) an accelerated main stream around the outer arch wall near the junctions of the left carotid and the left subclavian arteries, and (4) the vortices around the entrances of the three main branches. The study identifies and discusses the reasons for the flow physics' contribution to the formation of these features. The oscillating wall-shear stress distributions are closely related to the featured flow structures. On the outer wall of normal and slightly stenosed aortas, large wall-shear stresses appear in the regions upstream of the junction of the brachiocephalic artery as well as the corner near the junctions of the left carotid artery and the left subclavian artery. On the inner wall, the largest wall-shear stress appears in the region where the boundary layer separates.

List of symbols

A	Cross-section area of aorta model
B	Blockage ratio (=$[(E_2-R_i)/D_i] \times 100\%$)
De	Dean number (=$Re(r_i/R_c)^{0.5}$)
D_i	Inner diameter of aorta model, 25 mm
D_o	Outer diameter of aorta model, 28 mm
E_1	Short radius of ellipse for description of plaque
E_2	Long radius of ellipse for description of plaque
F	Frequency of flow pulsating
H	Length of straight sections of aorta model, 300 mm
P_{gage}	Gage pressure of pulsatile flow at upstream region
Q_{ave}	Time-averaged volumetric flow rate of pulsatile flow
Re_{ave}	Reynolds number based on average velocity (=$U_{ave}D_i/v$)
Re_{peak}	Reynolds number based on peak velocity of cardiac cycle
R_i	Radius of curvature of inner arch wall, 13.5 mm
r_i	Inner radius of aorta model cross section, 12.5 mm
R_c	Radius of curvature of centerline of arch, 27.5 mm
R_o	Radius of curvature of outer arch wall, 41.5 mm
r_o	Outer radius of aorta model cross section, 14 mm
T	Pulsating period of flow
t	Time evolution
t^*	Non-dimensional time (=t/T)

R. F. Huang (✉) · Y.-K. Lan
Department of Mechanical Engineering, National Taiwan
University of Science and Technology,
10672 Taipei, Taiwan, ROC
e-mail: rfhuang@mail.ntust.edu.tw

T.-F. Yang
Department of Biological Science and Technology, National
Chiao Tung University, 30068 Hsinchu, Taiwan, ROC
e-mail: 27342@sym.com.tw

U_{ave}	Time-averaged flow velocity of pulsatile flow ($=Q/A$)
u	Axial velocity
u_τ	Friction velocity ($=(\tau/\rho)^{1/2}$)
$u+$	Non-dimensional axial velocity ($=u/u_\tau$)
y	Coordinate normal to and away from wall
$y+$	Non-dimensional distance from wall ($=u_\tau y/v$)
α	Womersley parameter ($=r_i(f/v)^{0.5}$)
τ	Wall-shear stress
ρ	Density of working fluid ($=1.13$ g/cm^3 at 37°C)
v	Kinematic viscosity of working fluid ($=3.93 \times 10^{-6}$ m^2/s at 37°C)

1 Introduction

It has been observed that atherosclerotic lesions develop preferentially in relation to vicinities of curvature and arterial branching, where blood flow patterns are complex and multi-directional (Nerem 1992; Ku et al. 1985). A large number of in vivo investigations (e.g., Nerem and Seed 1972; Helmlinger et al. 1991; Davis 1995) have demonstrated that wall-shear stresses induced by the fluid flow intricately regulate endothelial cell structure and function. Wall-shear stress plays an important role in maintaining the homeostasis of the artery wall. It regulates the interaction with blood components and is essential to the controlling of thrombus formations (Adams et al. 1983; Malek et al. 1999). Studying flow characteristics in the aortic system promotes a better understanding regarding both the development of atherosclerosis and its relationship to flow structure.

Numerous experimental and computational studies have been performed to elucidate characteristics of flow fields and to establish correlations between particular hemodynamic phenomena and the etiology of atherosclerosis in the aortic arch (e.g., Khalighi et al. 1983a, b; Yearwood and Chandran 1980; Chandran et al. 1984, 1985a, b; Pei et al. 1985; Yearwood and Chandran 1984; Lei et al. 1995; Shahcheraghi et al. 2002; Kim et al. 2004). It was found that the curvature of the aortic arch contributes to the enhancement of the secondary flow and flow reversal, and therefore elevates the wall-shear stress oscillations. The locations of elevated wall-shear oscillations correspond to the vessel wall regions where atherosclerotic formation or aneurysm frequently occurs.

When an aorta is stenosed by plaque, flow behavior undergoes complicated modification due to the deformity of the arch cross section. The developed wall-shear stress also changes and subsequently influences the progress of the atherosclerotic lesions. This study investigates the physiological pulsatile flows and the shear stresses in normal and stenosed transparent rigid models of the aortic arch without a twist angle. Because the diameter of real aorta changes within a 10% range during the systolic/diastolic cycle and the propagation speed of the pulsatile waves is much higher (about five times) than the maximum blood speed (Singh et al. 1978), the rigid models are, therefore, reasonably adoptable for the aortic arches. The real aortic arch has, on the average, a twist angle of 15°. According to Rodkiewicz et al. (1985), the blood flow distribution is practically independent of the twist angle of the aortic arch, and the slight changes in flow pattern as a function of twist angle do not have any direct physiological implications. The three-dimensional model (which fabrication will take a more complicated effort to fit the requirement of particle image velocimetry (PIV) measurement) thus seems not to be a dominating factor for the purpose of studying the flow of central plane cut view. Therefore, the plane models are used in this study.

2 Experimental methods

2.1 Apparatus and experimental conditions

The models simulating the aorta with or without stenosis correspond to 180° curved circular tubes with three main arterial branches, as shown in Fig. 1. The models are made of highly transparent glass. Three models are used: (1) the arch of the curved tube is normal, (2) the inner wall of the arch is stenosed by a 25% blockage ratio of plaque, and (3) the inner wall of the arch is stenosed by a 50% blockage ratio of plaque. All three models consist of four parts: an ascending aorta, an arch, a descending thoracic aorta, and three arterial branches. The inner diameters of the cross sections of the normal arch, the brachiocephalic artery, the left carotic artery, and the left subclavian artery are 25, 12.5, 7.0, and 7.0 mm, respectively. The above inner diameters of the aortic arch, brachiocephalic artery, left carotic artery, and left subclavian artery are used because they simulate average geometric dimensions of normal human aortic systems. The length h of the ascending aorta and the descending thoracic aorta is 300 mm. The length of the three branches is 75 mm. The cross section of the arch is not exactly circular owing to technical difficulties affecting the fabrication. The side view of the cross section across the mid-plane of the arch looks like a near-circle "ellipse" with a little difference (about 2 mm) in long and short axes. Besides, the radius of curvature of the cross section at the inner arch is a little smaller than that at the outer arch. The inner and outer radiuses of curvature at the arch are $R_i = 13.5$ mm and $R_o = 41.5$ mm, respectively. The radius of curvature of the centerline thus is

Fig. 1 Geometry of simulated aorta models

Fig. 2 Arrangement of experimental setup

$R_c = 27.5$ mm. The ratio between the inner radius of the aorta cross section and the radius of curvature of the centerline, therefore, is $\delta = 0.45$, which approximates the value of 0.42 of human aorta. The plaque in the arch is best described as a section of an ellipse with short and long radiuses E_1 and E_2, respectively, as shown by the dashed-lines of Fig. 1. The blockage ratio is defined as $B = [(E_2 - R_i)/D_i] \times 100\%$, where D_i is the inner diameter of the aorta. The aorta model is completely immersed in a rectangular cross-section glass tank filled with an aqueous glycerol solution (the viscosity and temperature of which are the same as those of the working fluid described below) to reduce the image distortion induced by the light-deflection effects of the circular arc.

The model aorta is interconnected to a pulsatile flow supply system that consists of a pulsatile pump (Harvard Apparatus, Model 1423), a flow conditioner, a pressure transducer, a turbine flow meter, a water tank, several needle valves, rotameters, and certain piping components, as shown in Fig. 2. Sponges are inserted in the hydraulic piping at the location downstream the exit of the pulsatile pump, and a needle valve is installed downstream the exit

of the aortic arch to adjust the pressure at the inlet of the arch and to simulate the impedance of the systemic circulation, respectively. A mixture of glycerin in distilled water with a kinematic viscosity v of 3.93×10^{-6} m²/s and a density ρ of 1.13 g/cm³ at 37°C serves as the blood analog fluid (the temperature maintained throughout these experiments). Pulsatile flows simulating the output of a human heart beat are supplied by a "pulsatile pump". The stroke rate, stroke volume, and systole/diastole ratio are adjusted to 72 strokes/minute (1.2 Hz), 70 mL/stroke, and 45%/55%, respectively. The time-averaged flow rate Q_{ave} and the velocity U_{ave}, therefore, are 5.04 L/min and 0.17 m/s, respectively. The Womersley parameter α (Nerem and Seed 1972), the Dean number De (Dean 1927), and the time-averaged Reynolds numbers Re_{ave} are thus 17.31, 725, and 1,081, respectively. The peak velocities of the normal, 25, and 50% stenosed aortic arches are 0.39, 0.54, and 0.62 m/s, respectively. The Reynolds numbers based on the peak velocities of the normal, 25, and 50% stenosed aortic arches are, therefore, 2,484, 3,456, and 3,931, respectively. The flow rates of the passages through the brachiocephalic artery, the left carotic artery, and the left subclavian artery are adjusted to 11, 7.8, and 4.4% of the total flow rate, respectively, by means of needle valves and rotameters connected downstream of the three branches.

2.2 PIV measurement

A high-speed PIV system serves to measure the unsteady flow structure. The system consists of an infrared pulsing laser, a high-speed CMOS camera, an electronic synchronizer, and a notebook computer installed with sequence control, image acquisition, and PIV analysis software. The infrared laser can be externally triggered at either the single-pulsing mode or the double-pulsing mode at a wave length of 795 nm. The flash duration of each pulsing light is about 10 ns. The laser-light beam is expanded into a light sheet of a thickness smaller than 0.5 mm. The maximum camera speed is 2,000 fps at full resolution. The single-pulsing mode is used because the camera speed can fulfill the required pulse separation of 750 µs for this study. When the flow field of the whole aortic arch is measured (in order to observe the evolution of flow characteristics), the pixel array ($1,280 \times 1,728$) of the CMOS camera is mapped to a physical region of approximately 80 mm of side length so that the spatial resolution is about 70 µm/pixel. Plastic particles made of polyamide with a diameter of 5 ± 1.2 µm and a specific weight of 1.03 are seeded in the water tank to scatter the laser light.

Because the particle images would experience optical aberrations in a radial direction owing to the curved glass tubes, an image calibration serves to correct the measurement error induced by such aberrations (Huang et al. 2009). When the aorta model is filled with the working fluid and immersed in the aqueous glycerol solution contained in the rectangular cross-section glass tank, a precision rule is inserted into the transparent tube at the central plane, and a second precision rule is placed outside the tube. The images of the two precision rules are simultaneously photographed by a high-resolution digital camera. By comparing the difference in radial direction between the two precision scales, one obtains the calibration curve. The PIV-measured radial velocities are corrected accordingly.

Two consecutive image frames are analyzed by means of a cross-correlation technique (Keane and Adrian 1992) imbedded in the PIV analysis software. The software calculates the average displacement of local groups of particles in consecutive images. The interrogation window is set to 16×16 or 32×32 pixels. The displacement of the consecutive images relative to the length of the interrogation area is held to be smaller than 1/4 as suggested by Keane and Adrian (1990) to reduce velocity bias in the regions of large velocity gradients. The seeding density is adjusted to keep the number of particle-image pairs per interrogation spot no less than four so that the measurement reliability would not become significantly poor. The number of vectors (the grids) predetermined for the PIV analysis results is set to 6,084. Error check and interpolation routines serve to identify outliers and regenerate interpolated values to replace the identified outliers. The percentage of outliers in a vector map usually depends on factors such as seeding density, seeding homogeneity, out-of-plane motion, pulse separation, and analysis parameters such as the size of interrogation area. Even for well-optimized PIV images, which are analyzed with appropriate parameters, there is still a finite probability of getting some outliers. In general, this study obtains less than 1% of spurious vectors per instantaneous field. The general-purpose interpolation kernel, which uses nearest 8 or 24 neighbor values for processing, is optimized for vector maps with a 50% overlap of the interrogation and the interpolation algorithm. The method of interpolation is based on a weighted mean technique that replaces the values at filtered sites in an iterative manner by replacing those with the most surrounding valid values first, then working toward those that are less favorably positioned for accurate and reliable interpolation.

3 Results and discussion

3.1 Inlet pressure and pressure drop across arch

Figure 3 shows typical temporal variations of inlet pressures of the three aorta models. The inlet pressures are measured by means of a differential type piezoresistor pressure transducer installed at a position 3 cm upstream from the aorta model. The symbol P_{gage} denotes the gage pressure, t denotes the time evolution, and t^* is the normalized time t/T, where T is the period of pulsatility ($T = 0.83$ s in this study). The maximum pressures occur within the systolic phase. Toward the end of the systolic phase, the gage pressure decreases to negative values. In the case of the normal aorta, as shown in Fig. 3(a), the maximum inlet gage pressure attains about 12 kPa. While for the 25 and 50% stenosed aortas (Fig. 3b, c, respectively), the peak inlet pressures are raised slightly and attain about 14 kPa due to the increase of back pressure induced by the stenosis at the arch. The inlet pressures remain negative during the leading period of the diastolic phase and increase to positive values after the mid-period of the diastolic phase. The black dots marked on the curves of the pressure waves denoted by the letters a–h represent some critical instants that will be discussed in the following sections. The pressure drops across the arch of the three aorta models, as shown in Fig. 4, are measured by means of a differential type pressure transducer. The two pressure taps used to measure the pressure difference are respectively located at 3 cm upstream and downstream from the aorta model. The maximum pressure drop across the normal aortic arch attains about 5.5 kPa. While the maximum pressure drops of the stenosed aortas are increased by about
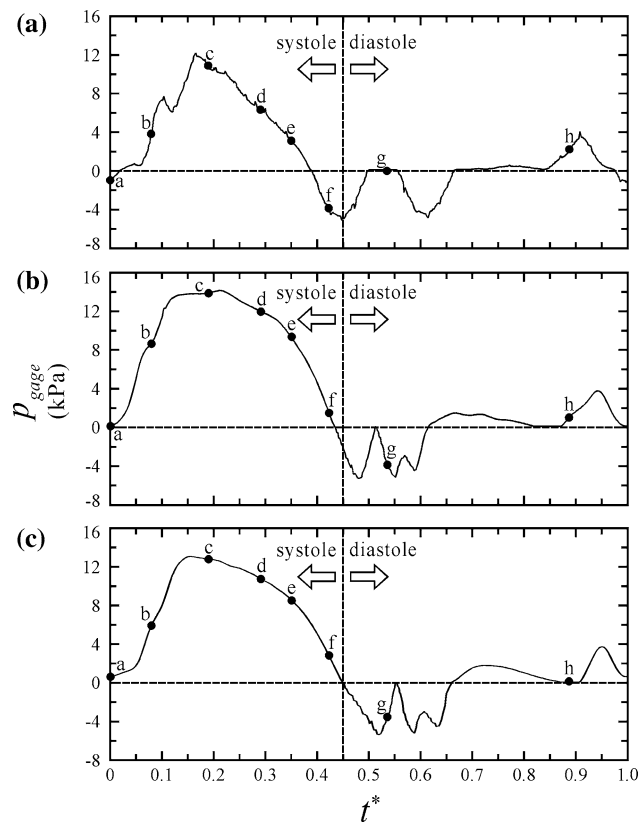
Fig. 3 Typical pressure wave cycle simulating physiological pressure output of heart beat. *Letters* a–h denote timings corresponding to subfigures (a–h) in Figs. 6, 7, 8. **a** normal arch, **b** 25% stenosed arch, **c** 50% stenosed arch
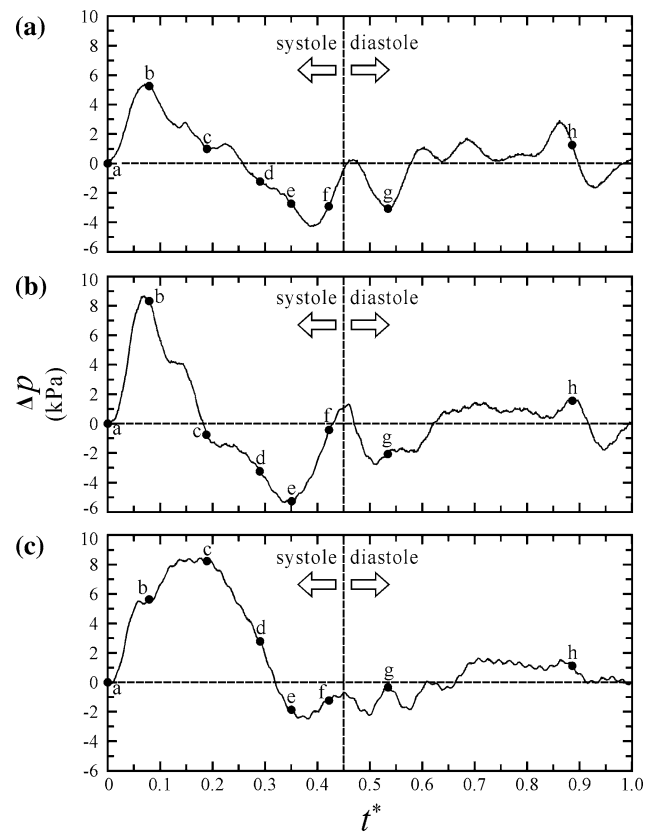

Fig. 4 Pressure drops across aorta arches. **a** normal arch, **b** 25% stenosed arch, **c** 50% stenosed arch

60% to a value of 9 kPa due to the blockage effect of the stenosis at the arch.

The instantaneous cross-section-averaged flow rates going through the three aorta models, as shown in Fig. 5, are measured by means of a calibrated turbine flow meter. The flow rate variations look much smoother than the pressure evolutions. The peak flow rates for the normal, 25% stenosed, and 50% stenosed aortic arches are 11.5, 16, and 18.2 L/min, respectively. These flow rates are also verified by integrating the instantaneous velocity distributions (obtained from PIV measurements) over the tube cross section. The difference is less than 5%.

3.2 Evolution of flow pattern

Each flow map in Figs. 6, 7, and 8 represents an ensemble average of over eighty instantaneous measurements at the same phase angle of each cardiac cycle. By this method, turbulence effects are averaged, and most of the streamtraces are smoothed so that large structures in the flow can be revealed clearly.

Figure 6 shows the selected time-evolving flow patterns in the central plane of the normal aorta model. As shown in

Fig. 6a through c (the acceleration period and the leading deceleration period of the systolic phase), the flow goes through the ascending aorta, the arch, and the descending thoracic aorta without any separation. Part of the flow goes into the three branches when the main flow passes through the arch. Throughout the acceleration period, the unsteady force associated with the acceleration of flow is positive, which enhances the inertial force and thereby overcomes the adverse pressure gradient induced by the large curvature of the arch. During the beginning period of deceleration, although the unsteady force becomes negative, the inertial effect can still overcome the combined effect of unsteady force and an adverse pressure gradient. Therefore, the streamtraces comply with the arch wall without showing any flow reversal. The centrifugal force developed by the turn-around motion of the flow should induce a counter-rotating secondary (helical) flow in the core region of the cross-section plane (Yearwood and Chandran 1984). During the mid-period of the systolic phase, as shown in Fig. 6d, e, counterclockwise-rotating vortices appear at the entrances of the three branching arteries, and this appearance implies that there are reverse flows around the left walls of the three branches. At $t^* = 0.350$, since the inertia can no longer resist the combined effect of the adverse
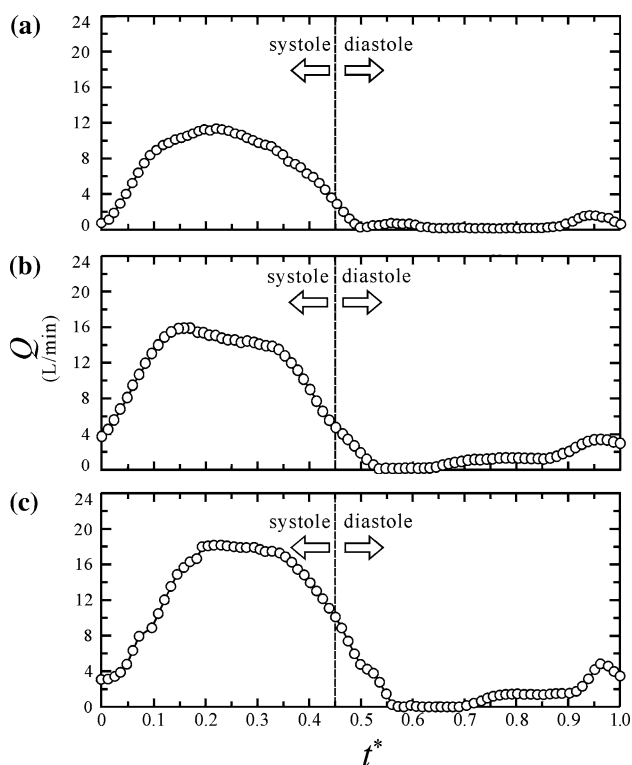
Fig. 5 Flow rate variations during a heart beat cycle. **a** normal arch, **b** 25% stenosed arch, **c** 50% stenosed arch

pressure gradient and negative unsteady force, reverse flow is found near the right inner wall of the arch. In Fig. 6(f), for the final stage of the systolic phase, the reverse flow along the left wall of the brachiocephalic artery extends to the left outer wall of the arch. So that the flow topology is satisfied, a recirculation bubble and a four-way saddle are formed around the left outer wall of the arch. The left carotid and the left subclavian arteries are filled with reverse flows. Simultaneously, the reverse-flow region near the inner wall of the arch enlarges. The cyclic procedure of the forward flow, the counterclockwise-rotating vortices, and the reverse flow at the entrances of the branching arteries may have opportunities to cause atherosclerosis and thrombosis, as pointed out by DeBakey et al. (1985). Flow separation can be observed in the region near the inner wall upstream of the arch. During the beginning period of the diastolic phase, as shown in Fig. 6g, the large flow structures keep enlarging, but present patterns not as coherent as those shown in Fig. 6f because of the decrease in the main-stream momentum. During the final period of the diastolic phase, as shown in Fig. 6h, the featured flow structures evolve and disappear.

Figure 7 shows the time-evolving flow patterns in the central plane of the 25% stenosed arch. During the acceleration period of the systolic phase, as shown in Fig. 7a, b, the flow behaves similarly to that in the normal aorta: it
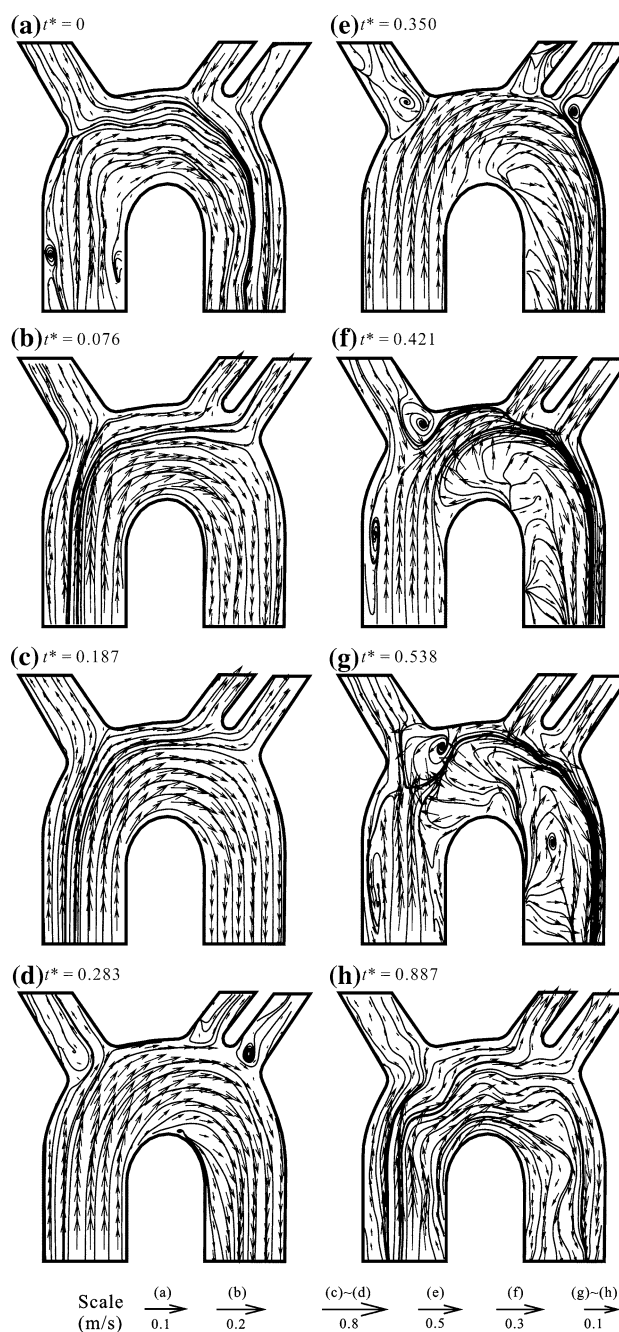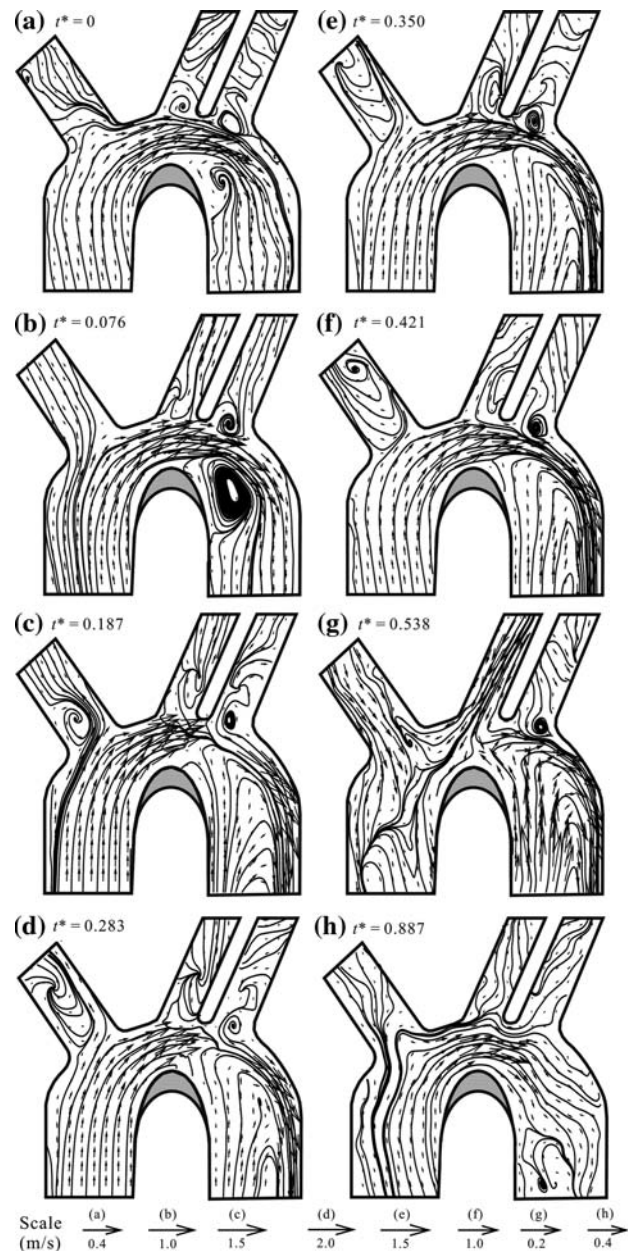

Fig. 6 Time-evolving process of velocity vectors and streamtraces in central plane of aorta model with normal arch

goes through the ascending aorta, the arch, and the descending thoracic aorta without any separation. In the leading deceleration period of the systolic phase, as shown in Fig. 7c, vortices appear around the entrances of the three branches: boundary-layer separation occurs from the apex of the plaque. In other words, these flow features in the stenosed aorta appear earlier than those in the normal aorta (which are observed during the mid-period of the systolic phase). During the mid-period of the systolic phase, as
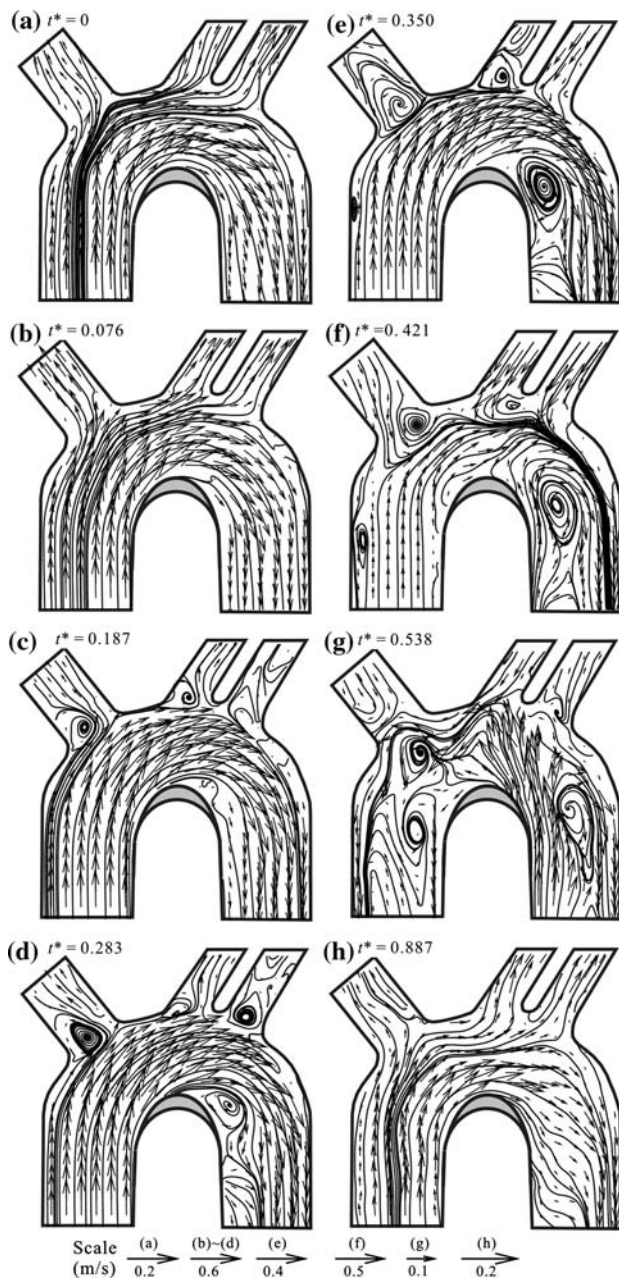
Fig. 7 Time-evolving process of velocity vectors and streamtraces in central plane of aorta model with 25% stenosed arch

Fig. 8 Time-evolving process of velocity vectors and streamtraces in central plane of aorta model with 50% stenosed arch

shown in Fig. 7d, e, the vortices located around the entrances of the three branches enlarge and almost block the entrances. The separated boundary layer evolving from the apex of the plaque develops into large, coherent vortex plaque during the mid- and final periods of the systolic phase, as shown in Fig. 7c through f. The separation bubble occupies a large part of the passage downstream of the plaque so that the main flow is "pushed" outwards when the main flow passes through the downstream half of the arch. The streamtraces around the outer right corner of the arch therefore look "dense." The flow velocity around that

area must increase if the continuity rule is to hold. During the diastolic phase, the flow presents similar behaviors to those in the normal aorta.

Figure 8 shows the time-evolving flow patterns in the central plane of the 50% stenosed arch. The vortices appearing around the entrances of the branches and the vortex induced by boundary-layer separation from the apex of the plaque can be observed even during the acceleration period of the systolic phase. These flow features persist throughout the deceleration period of the systolic phase. Traces of these flow features can still be found during the diastolic phase. The sizes of the vortices created in the flow

field of the 50% stenosed aorta become much larger than those in the normal and 25% stenosed aorta. The vortex evolving from the apex of the plaque, because of the boundary-layer separation, presents an extraordinarily large size; therefore, the streamtraces near the outer right wall of the arch look drastically dense.

Figure 9 shows the axial velocity profiles in the central plane of the normal and 50% stenosed aorta during the leading and final deceleration periods of the systolic phase. For the normal aorta at $t^* = 0.187$, the axial velocities at the stages A through K near the inner wall have larger values than those near the outer wall because the flow is making a 180° turn. The boundary-layer thickness on the inner wall is smaller than that on the outer wall. After the turn, as shown in the stages L through M, the axial velocities in the core region of the descending thoracic aorta recover to relatively uniform distributions. The boundary-layer thickness on the inner wall becomes larger than that on the outer wall. For the 50% stenosed arch at $t^* = 0.187$, the axial flow velocities near the inner wall of the final section of the ascending aorta (A through C) increase but not as substantially as those in the normal aorta because the turning angle in the upstream half of the arch declines owing to the existence of the plaque. As the flow makes the turn in the upstream half of the arch (D through G), the axial velocities drastically increase. At the mid-section across stage G, the axial flow behaves like a jet emerging from the gap between the apex of the plaque and the outer wall. In the downstream half of the arch and the descending thoracic aorta (H through M), the velocities near the inner wall present negative values because there exists a large recirculation bubble as shown in Fig. 8c. For the normal aorta at $t^* = 0.421$, negative axial flow velocities are found both near the outer wall of stages B through E and the inner wall of stages D through L. For the 50% stenosed arch at $t^* = 0.421$, the axial flow velocities are positive in the upstream half of the aorta because no flow separation occurs. In the downstream half of the aorta, negative axial velocities are found near the inner wall. The axial velocities and the velocity gradient near the outer wall at stages J through L are tremendously high. These high velocity gradients may induce large wall-shear stress around the right upper corner of the arch.
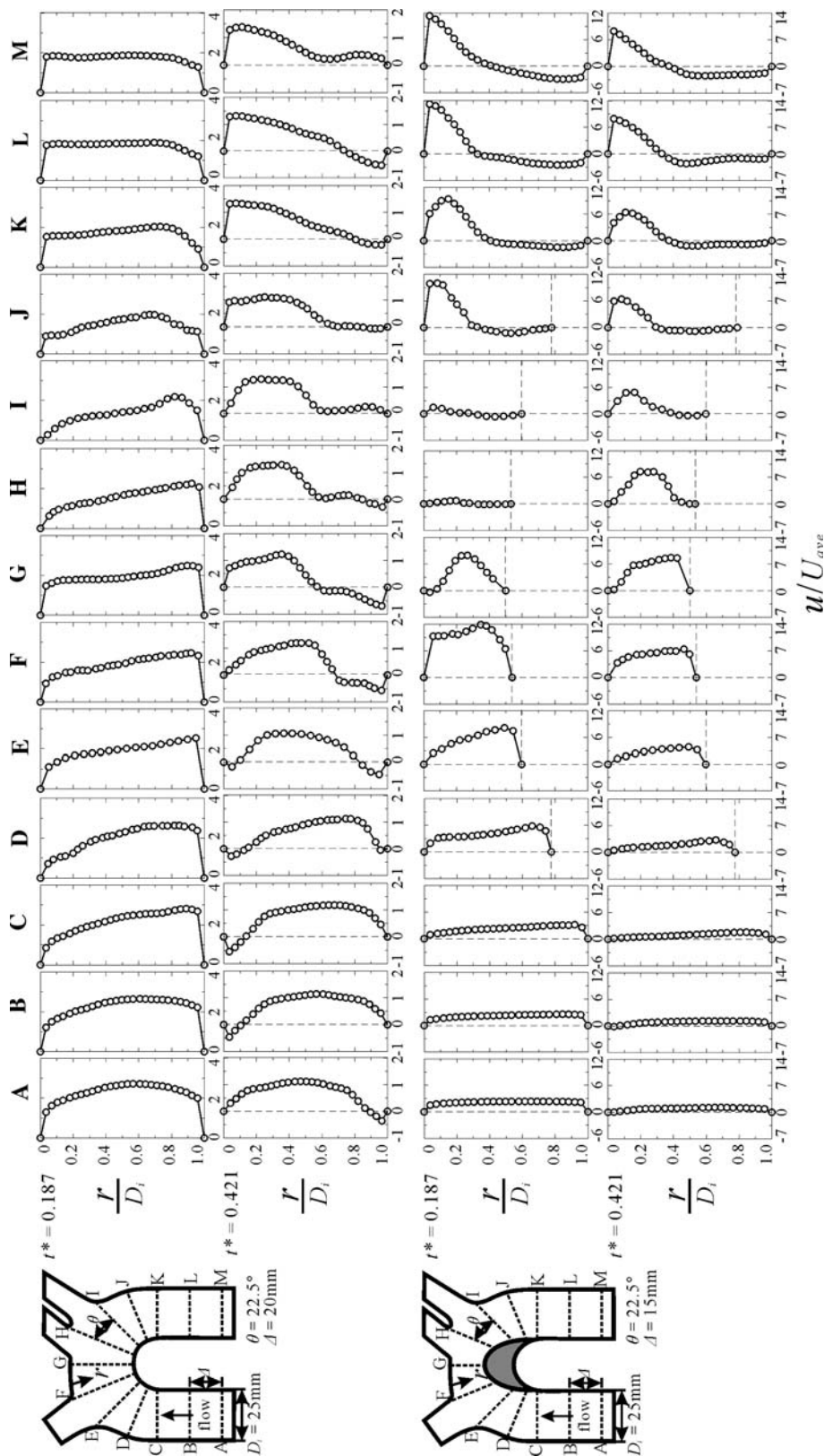
3.3 Wall-shear stress

The wall-shear stress distributions can be calculated by reference to the velocity data measured near the wall. It is a friction force per unit area asserted on the wall induced by the flowing fluids. Since the turbulent boundary layer on the wall of the aorta corresponds to complicated conditions (straight tube, arch curvature, and reverse flow), calculation of the wall-shear stress requires more consideration. The

camera's field of view zooms in to cover the area near the wall by about 1.8 mm × 1.8 mm so that the distance nearest the wall where the high accurate velocity data are obtained is approximately 0.15 mm away from the wall. This distance corresponds to the non-dimensional distance y^+, which is usually termed the Reynolds number based on the distance away from the wall and the friction velocity (Tennekes and Lumley 1972), about 6–8. This non-dimensional distance is located in the buffer zone of the turbulent boundary layer. A typical example of measurement in the flow region upstream the arch is shown in Fig. 10a. Because the measured velocity data are not in the viscous sublayer where $y^+ < 5$ (sometimes it is called the linear sublayer), it thus is improper to calculate the wall-shear stress directly by using the Newton's viscosity law. One may consider use the Clauser's method (Rohsenow and Choi 1961; Kays and Crawford 1980). However, since the present study deals with pipes including both straight and curved sections, the pressure gradient and flow separation require more profound considerations if the Clauser's method is to be used. Previous experiments (Huang and Bradshow 1995; Clauser 1954) show that the pressure gradient has a strong effect on the "law of wall for temperature" but nearly no effect on the "law of wall for velocity", the influence of the arch curvature on the near-wall flow structures of the turbulent boundary layer could be deemed insignificant. Therefore, in this study, the wall-shear stresses at the stages without boundary-layer separation (for both the straight and arch areas) are calculated with Clauser's method. That is, by using the velocity data measured in the range $y^+ = 30$–120 of the logarithmic sublayer, the friction coefficients can be calculated implicitly with the formula of logarithmic form. The friction coefficients are then converted into wall-shear stresses. For the regions with boundary-layer separation, special consideration has to be taken. Simpson et al. (1981) and Adams and Johnston (1988) reported the flow structure in the near-wall zone of a turbulent separated flow. They concluded that the shear stress throughout the separated boundary layer is predominantly viscous, i.e., the flow appears to be "laminar-like" from the wall out to the region of the maximum local backflow velocity, even though the fluctuation levels are very high. The velocity data obtained in this study in the regions with separated boundary layers, as shown in Fig. 10b, support the results of Simpson et al. and Adams and Johnston. Therefore, Newton's viscosity law (i.e., linear law) is used to calculate the wall-shear stresses for the stages with flow separation.

Figure 11 shows the wall-shear stress exerting itself on the outer (left column) and inner (right column) walls of the normal aorta. The wall-shear stresses exhibit oscillation during the cardiac cycle: positive in the systolic phase and negative in the diastolic phase. On the outer wall, as shown

Fig. 9 Axial velocity distributions in central plane of aorta model with normal arch (*upper two rows*) and 50% stenosed arch (*lower two rows*)


in Fig. 11a, b, the shear stresses attain maximum values at $t^* \approx 0.3$, which happens during the mid-deceleration period of the systolic phase. In the regions A through C

and H through J, the wall-shear stresses are particularly high. The A–C region is located around the end section of the ascending aorta, where the reverse flow-induced
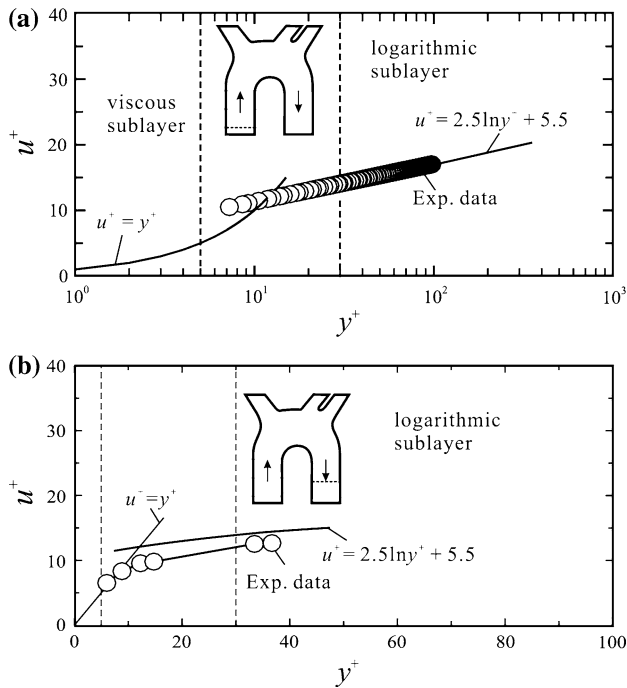
Fig. 10 Velocity profiles measured in boundary layer. **a** in forward flow region, at $t^* = 0.137$ across *dashed lines*, and **b** in separated flow region, at $t^* = 0.421$ across *dashed lines*
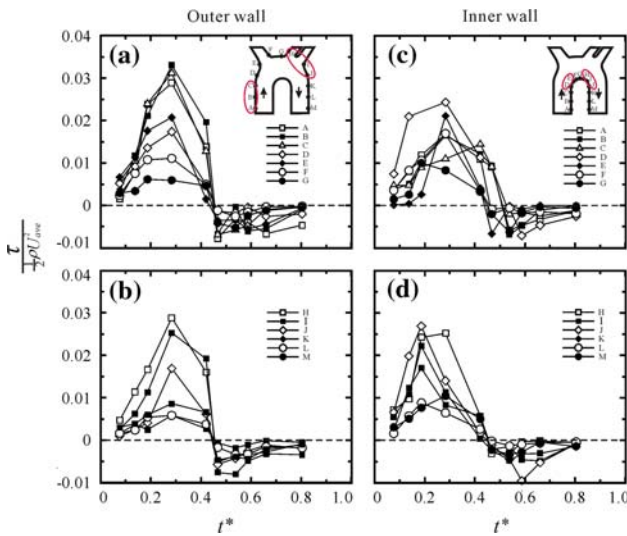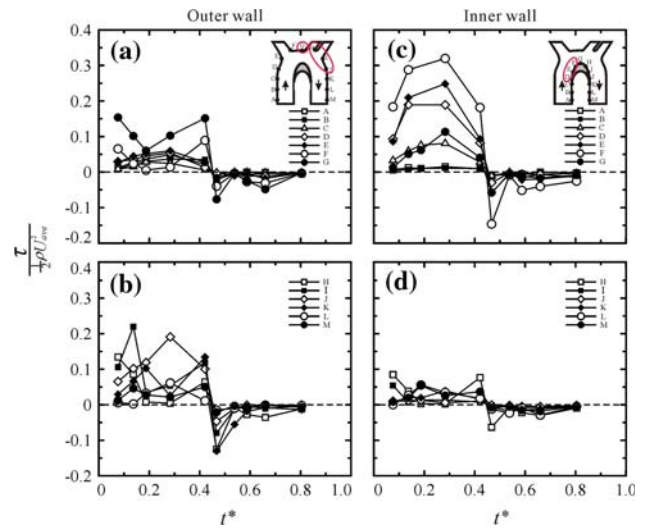

Fig. 11 Wall-shear stress distributions of normal aorta. **a**, **b** outer wall, **c**, **d** inner wall

recirculation vortex appears, as shown in Fig. 6f, g. The H–J region is located around the right downstream corner of the arch, where the main flow is accelerated by the deflection effect of the recirculation bubble, as shown in Fig. 6f, g. On the inner wall, as shown in Fig. 11c, d, large wall-shear stresses appear around the D–E stages (the upstream turning corner of the arch) and the H–K stages (the downstream turning corner of the arch). The D–E
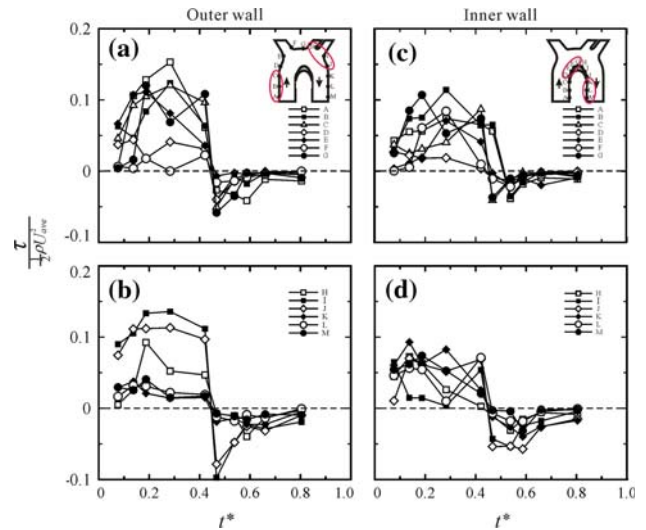
Fig. 12 Wall-shear stress distributions of 25% stenosed aorta. **a**, **b** outer wall, **c**, **d** inner wall

Fig. 13 Wall-shear stress distributions of 50% stenosed aorta. **a**, **b** outer wall, **c**, **d** inner wall

region is located at the boundary-layer separation region, as shown in Fig. 6f, g. These regions with high wall-shear stress correspond to the areas that are vulnerable to types I, II, and III aortic dissection and dissecting aneurysms as reported by DeBakey et al. (1982).

As the arch is stenosed, the values of wall-shear stresses at all stages are drastically escalated, as shown in Fig. 12 (25% stenosis) and 13 (50% stenosis). In the 25% stenosed aorta, as shown in Fig. 12, large values of wall-shear stress occurring on the outer wall are located in the A–C and H–J regions, and these values are the same as those observed in the case of normal aorta. On the inner wall, regions of large wall-shear stress are shifted to the D–G and K–M regions. The apex G of the plaque presents particularly large oscillating stresses

during the systolic and diastolic phases. The apex point G is located where the boundary layer separates, as shown in Fig. 7c through e. In the 50% stenosed aorta, as shown in Fig. 13a, b, large wall-shear stresses on the outer wall are located at G and in the H–J region. On the inner wall, as shown in Fig. 13c, d, the high shear stresses appear in the D–F region, which is located around the upstream corner of the plaque. It is obvious that once the stenosis is formed in the aortic arch, the elevated oscillating wall-shear stresses applying to the outer wall at the same vulnerable regions as those experienced both in the normal aorta and in the regions upstream and downstream of the plaque may have profound effects on the further development of aortic dissection or atherosclerotic formation.

4 Conclusions

Three flow structures characterize the flow patterns in the central plane of the normal or stenosed aortic arch during the aortic cycle. A large separation bubble around the inner arch wall is induced by the large adverse pressure gradient. A recirculation vortex around the outer arch wall upstream of the junction of the brachiocephalic artery is induced by the reverse flow from the brachiocephalic artery during the deceleration period of the systolic phase and the diastolic phase. The main stream around the outer arch wall near the junctions of the left carotid and the left subclavian arteries accelerates owing to the blockage effect of either the stenosis or the separation bubble. The vortices around the entrances of the three main branches are induced by boundary-layer separation at the inlets of branching arteries. The wall-shear stress distributions are closely related to these characteristic flow structures. On the outer wall of normal or slightly stenosed aorta, large wall-shear stresses appear in two regions. One region is located upstream of the junction of the brachiocephalic artery: the large wall-shear stress is due to the recirculation bubble, and the recirculation bubble is due to the flow reversal from the brachiocephalic artery. The other region is around the right upper corner near the junctions of the left carotid artery and the left subclavian artery: the large wall-shear stress is due to the acceleration of the main flow, and the main flow acceleration is due to the boundary-layer separation from the inner arch wall. These regions with high wall-shear stress correspond to the areas that are vulnerable to aortic dissection and dissecting aneurysms. In the severely stenosed aorta, the largest shear stress on the outer wall would appear around the top of the arch: the large shear stress is due to the deflected stream, and the stream deflection is due to the plaque. On the inner wall, large wall-shear stress appears in the region where the boundary layer separates. Even a small stenosis appearing in the arch would induce

drastic escalation of wall-shear stresses in the same regions where the normal aorta experiences. Severe stenosis would cause the locations of the large wall-shear stresses to shift.

References

Adams EW, Johnston JP (1988) Flow structure in the near-wall zone of a turbulent separated flow. AIAA J 26(8):932–939
Adams GA, Brown SJ, McIntire LV, Eskin SG, Martin RR (1983) Kinetics of platelet adhesion and thrombus growth. Blood 62:69–74
Chandran KB, Cabell GN, Khalighi B, Chen C-J (1984) Pulsatile flow past aortic valve bioprostheses in a model human aorta. J Biomech 17(8):609–619
Chandran KB, Khalighi B, Chen C-J (1985a) Experimental study of physiological pulsatile flow past valve prostheses in a model of human aorta—I. Caged ball valves. J Biomech 18(10):763–772
Chandran KB, Khalighi B, Chen C-J (1985b) Experimental study of physiological pulsatile flow past valve prostheses in a model of human aorta—II. Tilting disc valves and the effect of orientation. J Biomech 18(10):773–780
Clauser FH (1954) Turbulent boundary layers in adverse pressure gradient. J Aeronaut Sci 21(2):91–108
Davis PF (1995) Flow-medicated endothelial mechanotransduction. Physiol Rev 75:519–560
Dean WR (1927) Note on the motion of fluid in a curved pipe. Phil Mag 20:208–223
DeBakey ME, McCollum CH, Grawford ES, Morris GC, Howell J, Noon GP, Lawrie G (1982) Dissection and dissecting aneurysms of the aorta: twenty-year follow-up of five hundred twenty-seven patients treated surgically. Surgery 92(6):1118–1134
DeBakey ME, Lawrie GM, Glaeser DH (1985) Patterns of atherosclerosis and their surgical significance. Ann Surg 201(2):115–131
Helmlinger G, Berk RV, Schrech S, Nerem RM (1991) Effects of pulsatile flow on cultured vascular endothelial cell morphology. J Biomech Eng 113:123–134
Huang PG, Bradshow P (1995) Law of the wall for turbulent flows in pressure gradients. AIAA J 33(4):624–632
Huang RF, Lin KH, Yeh C-N (2009) In-cylinder tumble flows and performance of a motorcycle engine with circular and elliptic intake ports. Exp Fluids 46(1):165–179
Kays WM, Crawford ME (1980) Convective heat and mass transfer. McGraw-Hill, New York
Keane RD, Adrian RJ (1990) Optimization of particle image velocimeters Part I: double pulsed systems. Meas Sci Technol 1(6):1202–1215
Keane RD, Adrian RJ (1992) Theory of cross-correlation analysis of PIV images. Appl Sci Res 49(3):191–215
Khalighi B, Chandran KB, Chen C-J (1983a) Steady flow development past valve prostheses in a model human aorta—I. Centrally occluding valves. J Biomech 16(12):1003–1011
Khalighi B, Chandran KB, Chen C-J (1983b) Steady flow development past valve prosthese in a model human aorta—II. Tilting disc valves. J Biomech 16(12):1013–1018
Kim T, Cheer AY, Dwyer HA (2004) A simulated dye method for flow visualization with a computational model for blood flow. J Biomech 37(12):1125–1136
Ku DN, Giddens DP, Zarins CK, Glagov S (1985) Pulsatile flow and atherosclerosis in the human carotid bifurcation: positive correlation between plaque location and low and oscillating shear stress. Arteriosclerosis 5(3):293–301

Lei M, Kleinstreuer C, Truskey GA (1995) Numerical investigation and prediction of atherogenic sites in branching arteries. J Biomech Eng 117(8):350–357

Malek AM, Alper SL, Izumo S (1999) Hemodynamic shear stress and its role in atherosclerosis. J Am Med Assoc 282:2035–2042

Nerem RM (1992) Vascular fluid mechanics, the arterial wall and atherosclerosis. J Biomech Eng 114(8):274–282

Nerem RM, Seed WA (1972) An in vivo study of aortic flow distributions. Cardiovasc Res 6:1–14

Pei Z-H, Xi B-S, Hwang HC (1985) Wall shear stress distribution in a model human aortic arch: assessment by an electrochemical technique. J Biomech 18(9):645–656

Rodkiewicz CM, Kalita W, Kennedy JS, Pelot R (1985) On the flow field distributions due to the aortic arch twist. J Biomech 18(10):781–787

Rohsenow WM, Choi HY (1961) Heat, mass and momentum transfer. Prentice-Hall, Englewood Cliffs

Shahcheraghi N, Dwyer HA, Cheer AY, Barakat AI, Rutaganira T (2002) Unsteady and three-dimensional simulation of blood flow in the human aortic arch. J Biomech Eng 124(8):378–387

Simpson RL, Chew Y–T, Shivaprasad BG (1981) The structure of a separating turbulent boundary layer. J Fluid Mech 113(4):23–51

Singh MP, Sinha PC, Aggarwal M (1978) Flow in the entrance of the aorta. J Fluid Mech 87(1):97–120

Tennekes H, Lumley JL (1972) A first course in turbulence. MIT Press, Cambridge

Yearwood TL, Chandran KB (1980) Experimental investigation of steady flow through a model of the human aortic arch. J Biomech 13(4):1075–1088

Yearwood TL, Chandran KB (1984) Physiological pulsatile flow experiments in a model of the human aortic arch. J Biomech 15(9):683–704